Lossy transmission line response via numerical Laplace transform inversion

Band structure and optical anisotropy in *V*-shaped and *T*-shaped semiconductor quantum wires

G. Goldoni, F. Rossi, and E. Molinari
Istituto Nazionale per la Fisica della Materia (INFM)
and Dipartimento di Fisica, Università di Modena, Via Campi 213/A, I-41100 Modena, Italy

A. Fasolino
Istituto Nazionale per la Fisica della Materia (INFM),
Dipartimento di Fisica, Università di Modena, Via Campi 213/A, I-41100 Modena, Italy
and Institute of Theoretical Physics, University of Nijmegen, Toernooiveld, 6525 ED Nijmegen, The Netherlands
(Received 20 September 1996)

We present a theoretical investigation of the electronic and optical properties of *V*- and *T*-shaped quantum wires. Valence-band mixing as well as realistic sample geometries are fully included through an accurate and efficient approach that is described here in detail. We investigate the resulting valence-band structure, which shows some significant peculiarities, such as an anomalously large spin splitting in the lowest heavy-hole subband of *T*-shaped wires. For both classes of wires we obtain good agreement between calculated optical absorption and recent experimental spectra, and we demonstrate that the analysis of optical anisotropy can be used as an effective tool to extract information on valence states, which is usually very difficult to obtain otherwise. [S0163-1829(97)01008-4]

INTRODUCTION

In recent years, one-dimensional (1D) semiconductor nanostructures have received increasing attention. The potential technological application of quantum wires (QWR's), e.g., in laser devices, has fueled a search for new fabrication techniques and improved sample quality.[1] In this area, recent investigations have focused on two classes of structures, the so-called *V*-shaped[2–6] and *T*-shaped[7–14] QWR's (*V*-QWR's and *T*-QWR's). Due to high control on growth conditions and strong confinement of the electron and hole wave functions on the scale of a few nanometers, *V*-QWR's and *T*-QWR's share desirable optical properties for device applications, such as large exciton binding energy and a small linewidth.

V-QWR's are obtained from a GaAs substrate grown along the [001] crystallographic direction, patterned with [$\bar{1}$10]-oriented *V*-shaped grooves obtained by chemical etching. The active region consists of a GaAs layer cladded between two $Al_xGa_{1-x}As$ regions[2] or GaAs/AlAs superlattices[5] (SL's) overgrown on the patterned substrate. The confining potential (see Fig. 1) has a crescent shape profile. *T*-QWR's are obtained by first growing a $GaAs/Al_xGa_{1-x}As$ SL on a (001) substrate. After cleavage, a GaAs quantum well (QW) is grown over the exposed (110) surface, resulting in a *T*-shaped active region.[7] In both cases, the electron and hole wave functions are confined in the [001] and [$\bar{1}$10] crystallographic directions, while the QWR free axis is parallel to the [$\bar{1}$10] direction.

The optical spectroscopy of QWR's is more complex than for QW's of similar lateral dimension, since in QWR's linewidths can be comparable to intersubband splittings. On the other hand, a remarkable peculiarity of QWR's with respect to QW's is that the optical activity is strongly anisotropic when light is linearly polarized, with the electric field directed parallel or perpendicular to the wire axis. This has long been recognized to be a band structure effect due to the quasi-one-dimensional character of electronic state, combined with heavy- and light-hole (HH and LH) mixing.[15] The anisotropic absorption is therefore used as a simple tool to reveal the 1D character of electronic states in nanostructured materials.

In principle, the optical anisotropy can be exploited to single out detailed information on the electronic states, since, as we will show, it is very sensitive to specific details of the band structure. In practice, this approach has been so far limited by the lack of realistic calculations for complex geometries, as the present *V*-QWR's and *T*-QWR's. Indeed, common theoretical methods, even within semiempirical schemes as the tight-binding or the envelope-function approach, require a large scale computational effort. In order to keep calculations tractable, up to now the optical properties of QWR's have been investigated theoretically only for rather idealized structures,[16–21] yielding results that cannot be directly compared with experimental spectra. Calculations have been performed for realistic QWR geometries,[22] but they have so far neglected HH-LH mixing.

Recently, we have demonstrated, by a combined theoretical-experimental study of *V*-QWR's,[23] that accurate band structure calculations for realistic structures provide quantitative predictions of photoluminescence excitation (PLE) spectra, and that detailed information on the valence-band states can be singled out of the PLE anisotropy, despite the dominant role of the light conduction electrons in the optical spectra. Such calculations were based on a recently devised method which provides the band structure for QWR's of arbitrary geometry at a relatively small computational cost. The accuracy and the short computer times make such calculations a practical characterization tool in conjunc-

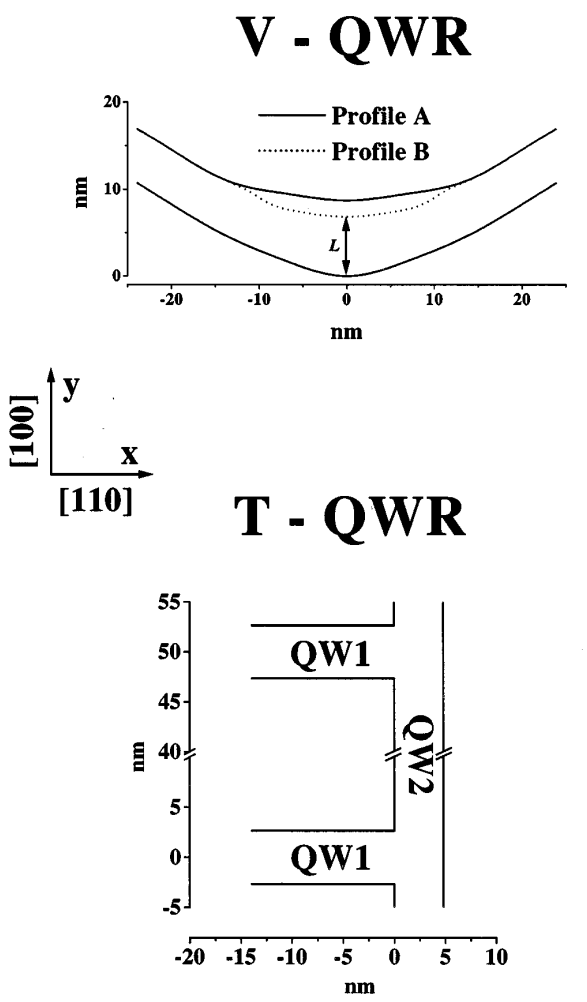

FIG. 1. Confining potential profiles of *V*-QWR's and *T*-QWR's, with an indication of relevant crystallographic directions and reference frame. For *V*-QWR's we show two potential profiles, profile *A* (solid line) and profile *B* (dotted line), which are characterized by a different value of the confinement length L (profile *A*: $L=8.7$ nm; profile *B*: $L=6.83$ nm) and which will be investigated in Sec. II; the supercell periodicity used in the calculations (see Sec. I) is approximately 120 nm along x and 37 nm along y. For the *T*-QWR, QW1 is truncated at the left-hand side at $x=-50$ nm; the supercell periodicity is approximately 55 nm along x and 50 nm along y.

tion with experimental results, as well as a predictive tool for new devices.

In this paper, we present a theoretical investigation of the electronic and optical properties of *V*-QWR's and *T*-QWR's. We focus on the relationship between optical anisotropy and band structure, and we show how the analysis of optical anisotropy permits a detailed spectroscopy of valence states, even when the large linewidth of the spectra does not allow an identification of the valence-to-conduction subband transitions. For *T*-QWR's we also predict a huge spin splitting of the lowest valence subband, originating from the interaction between the lowest HH levels of the intersecting QW's. For both classes of wires, calculations are performed by the numerical method introduced in Ref. 23—described here in detail—thereby demonstrating its accuracy and flexibility.

The main approximation that is still present in our approach is the neglect of excitonic effects. Indeed, recent calculations which fully include Coulomb interaction in realistic QWR profiles[22] (but do not include HH-LH mixing) demonstrate that electron-hole interaction, besides giving rise to bound excitonic states below the band edge, also modifies the excitonic continuum above the band edge. However, our previous investigation in *V*-QWR's (Ref. 23) has shown that quantitative agreement is obtained between the observed PLE anisotropy, which probe the excitonic continuum, and the anisotropy in absorption spectra calculated neglecting excitonic effects. We interpret this result as an indication that the electron-hole Coulomb interaction, by mixing isotropically the (optically anisotropic) electron and hole states, does not change the average anisotropy as obtained by single particle band structure calculations. This is of course compatible with the possibility that the relative intensity of the absorption peaks for a given polarization may be strongly affected.[17] The above arguments suggest that the approximation of neglecting electron-hole Coulomb coupling is a reasonable one for our purpose of studying optical anisotropies. Of course, its accuracy for the present *V*- and *T*-QWR's must be established *a posteriori* by comparison with experiments, as we will do later on in this paper.

The theoretical background and the numerical method used in our calculations are outlined in Sec. I. Sections II and III report the results of our calculations, focusing on the band structure and optical anisotropy, for *V*-QWR's and *T*-QWR's, respectively.

I. MODELING THE BAND STRUCTURE IN WIRES OF ARBITRARY GEOMETRY

In this section we describe the theoretical framework of our calculations. As we are interested in optical transitions near the direct band gap of GaAs, and because QWR electronic states are extended over several nanometers, we work within the envelope function approximation. For the wires of interest in this paper, we choose the following Cartesian reference frame (see also Fig. 1): x along the $[\bar{1}10]$ direction, y along the [001] direction, and z along the $[\bar{1}10]$ direction. Therefore, for both classes of wires, the QWR section extends in the $x-y$ plane, while its free axis is parallel to the z direction. Due to translational invariance, along this direction it is possible to define a 1D wave vector k_z. In the x and y directions we assume a supercell periodicity, i.e., we describe arrays of QWR's. The size of the supercell can be taken large enough to describe effectively isolated wires when needed.

Electron and hole states will be described separately by different effective mass equations. For conduction electrons, we assume a single-band approximation, which implies a parabolic energy dispersion in the free direction; the wave functions of the electron subbands are

$$\Psi_n^e(\mathbf{r})=F_n^e(\mathbf{r})|s,\sigma\rangle, \tag{1}$$

where $|s,\sigma\rangle$ is the atomic s state with spin $\sigma\in\{\uparrow,\downarrow\}$, n is the subband index, and $F_n^e(\mathbf{r})$ is the nth solution of the envelope-function equation. Since we deal with a two-dimensional confinement potential $V(x,y)$, we can factorize $F_n^e(\mathbf{r})=e^{ik_z z}\psi_n^e(x,y)$, where ψ_n^e is the nth solution of

$$\hat{H}^e \psi_n^e(x,y) = E_{n,k_z}^e \psi_n^e(x,y), \tag{2}$$

with the electron effective mass Hamiltonian

$$\hat{H}^e = \left[\frac{\hbar^2}{2m_e} (\hat{k}_x^2 + \hat{k}_y^2 + k_z^2) + V(x,y) \right]; \tag{3}$$

here m_e is the electron effective mass, and $\hat{k}_x = -i\partial/\partial x$, $\hat{k}_y = -i\partial/\partial y$. Of course, in this one-band description, the electron subbands E_{n,k_z}^e depend quadratically on k_z:

$$E_{n,k_z}^e = \epsilon_n^e + \frac{\hbar^2 k_z^2}{2m_e}, \tag{4}$$

where the ϵ_n^e's are the confinement energies (i.e., the subband edges). The subbands E_{n,k_z}^e are spin degenerate, and the ψ_n^e's are k_z independent.

Conduction-band states do not directly contribute to optical anisotropy, being mainly of isotropic s-type character, and in this case the above one-band description is sufficient. Conversely, it is essential to give an accurate account of p-type valence states by a multiband description, in order to investigate optical anisotropy. Due to mixing between HH and LH subbands, both eigenvalues and envelope functions depend nontrivially on the wave vector k_z and the hole subband index m. Using the compact notation $\alpha = (k_z, m)$, we write the hole wave functions

$$\Psi_\alpha^h(\mathbf{r}) = \sum_{J_m} F_{J_m,\alpha}^h(\mathbf{r}) |3/2, J_m\rangle, \tag{5}$$

where $|3/2, J_m\rangle$ are the four atomic states with total angular momentum $J = 3/2$ and projection $J_m = +3/2$, $+1/2$, $-1/2$, $-3/2$ of J along a quantization axis. Again, each envelope function $F_{J_m,\alpha}^h(\mathbf{r})$ can be factorized as $F_{J_m,\alpha}^h(\mathbf{r}) = e^{ik_z z} \psi_{J_m,\alpha}^h(x,y)$, and the four-component vector $\boldsymbol{\psi}_\alpha^h(x,y) = (\psi_{+3/2,\alpha}^h, \psi_{-1/2,\alpha}^h, \psi_{+1/2,\alpha}^h, \psi_{-3/2,\alpha}^h)$ is the mth solution at point k_z of the multiband effective mass equation,[24]

$$\hat{\mathbf{H}}_L \, \boldsymbol{\psi}_\alpha^h = E_\alpha^h \, \boldsymbol{\psi}_\alpha^h, \tag{6}$$

where $\hat{\mathbf{H}}_L$ is the Luttinger Hamiltonian.[25] With the above choice of coordinate axes and the quantization axis of **J** along the [110] direction, following Ref. 26 the Luttinger Hamiltonian reads

$$\hat{\mathbf{H}}_L = \frac{\hbar^2}{2m_0} \begin{pmatrix} \hat{P}_1 + V(x,y) & \hat{R} & \hat{Q} & 0 \\ \hat{R}^\dagger & \hat{P}_2 + V(x,y) & 0 & -\hat{Q} \\ \hat{Q}^\dagger & 0 & \hat{P}_2 + V(x,y) & \hat{R} \\ 0 & -\hat{Q}^\dagger & \hat{R}^\dagger & \hat{P}_1 + V(x,y) \end{pmatrix} \begin{matrix} |3/2,+3/2\rangle \\ |3/2,-1/2\rangle \\ |3/2,+1/2\rangle \\ |3/2,-3/2\rangle \end{matrix}, \tag{7}$$

where

$$\hat{P}_1 = \left(\gamma_1 - \frac{\gamma_2 + 3\gamma_3}{2} \right) \hat{k}_x^2 + (\gamma_1 + \gamma_2) \hat{k}_y^2 + \left(\gamma_1 - \frac{\gamma_2 - 3\gamma_3}{2} \right) k_z^2, \tag{8a}$$

$$\hat{P}_2 = \left(\gamma_1 + \frac{\gamma_2 + 3\gamma_3}{2} \right) \hat{k}_x^2 + (\gamma_1 - \gamma_2) \hat{k}_y^2 + \left(\gamma_1 + \frac{\gamma_2 - 3\gamma_3}{2} \right) k_z^2, \tag{8b}$$

$$\hat{R} = -\sqrt{3} \left[-\frac{\gamma_2 - \gamma_3}{2} \hat{k}_x^2 + (\gamma_2 \hat{k}_y - 2i\gamma_3 k_z) \hat{k}_y - \frac{\gamma_2 + \gamma_3}{2} k_z^2 \right], \tag{8c}$$

$$\hat{Q} = -2\sqrt{3} (\gamma_3 \hat{k}_y - i\gamma_2 k_z) \hat{k}_x. \tag{8d}$$

This Hamiltonian provides the (positive definite) hole subbands, referred to the bulk valence-band edge, as a function of the in-wire wave vector k_z, including HH-LH mixing. The hole Hamiltonian for structures grown along crystallographic directions different from the present ones can be obtained along the lines of Ref. 26. In the above electron and hole effective mass Hamiltonians we neglect the material dependence of the electron effective mass m_e and the Luttinger parameters γ_1, γ_2, and γ_3, and we always use the bulk GaAs values listed in Table I. Although our approach can be extended to account for the material dependence, this would be a small effect in our calculations.

One possible approach to solve the multiband equation (6) is to split the problem in two parts: the first step is to solve the two Schrödinger-like equations arising from the diagonal terms of (7),

$$[\hat{P}_1 + V(x,y)] \phi_i^1(x,y) = \epsilon_i^1 \phi_i^1(x,y), \tag{9}$$

$$[\hat{P}_2 + V(x,y)] \phi_i^2(x,y) = \epsilon_i^2 \phi_i^2(x,y). \tag{10}$$

The second step is to use the set ϕ_i^1 as a basis to expand the components $\pm 3/2$ of the vector $\boldsymbol{\psi}_\alpha^h$, and the set ϕ_i^2 as a basis for the components $\pm 1/2$. In this representation, the diagonal matrix elements of the $\mathbf{H}_L$ are given by the two sets of scalar numbers ϵ_i^1, ϵ_i^2, and matrix elements need only to be calculated for off-diagonal terms, using the functions ϕ_i^1, ϕ_i^2. This approach has the following drawback: since

TABLE I. Bulk GaAs band parameters used in the calculations.

m_e	γ_1	γ_2	γ_3	E_g (eV)
0.067	6.85	2.1	2.9	1.519

the effective masses appearing in $\hat{P}_1$, $\hat{P}_2$ (the so-called HH and LH effective masses) are very different, the two sets of eigenvalues ϵ_i^1, ϵ_i^2 span different energy ranges. The set ϵ_i^2, being the spectrum of a light particle, will have larger gaps, and the ground state will be higher in energy than for the set ϵ_i^1. Since we are mainly interested in the low-lying hole subbands near ϵ_1^1, this representation, although exact in principle, is poorly convergent with respect to the number of states ϕ_i^1, ϕ_i^2 included in the basis, and it is not practical in numerical calculations.

To solve this problem, we propose a scheme in which we expand the components of ψ_α using the solutions of two Schrödinger-like equations with two fictitious, arbitrary masses m^+, m^-, which we then tune in order to improve the convergence:

$$\left[\frac{\hbar^2}{2m^+}(\hat{k}_x^2+\hat{k}_y^2)+V(x,y)\right]\phi_\nu^+(x,y)=\epsilon_\nu^+\phi_\nu^+(x,y), \tag{11a}$$

$$\left[\frac{\hbar^2}{2m^-}(\hat{k}_x^2+\hat{k}_y^2)+V(x,y)\right]\phi_\mu^-(x,y)=\epsilon_\mu^-\phi_\mu^-(x,y) \tag{11b}$$

(here and in the following we use the index ν for $+$ states, and μ for $-$ states). In this way, we diagonalize exactly only *part* of the kinetic energy terms $\hat{P}_1$ and $\hat{P}_2$ of $\hat{\mathbf{H}}_L$, but the potential $V(x,y)$ is exactly diagonalized. Of course, in this representation ϵ_ν^+, ϵ_μ^- are *not* the diagonal elements of the matrix representing the Hamiltonian, and $\hat{P}_1$, $\hat{P}_2$ give rise to additional off-diagonal terms. However, the time spent to calculate the additional terms is more than compensated by the improved convergence which can be achieved by properly choosing m^+ and m^-. In the end, we shall find it convenient to choose $m^+=m^-$, and both equal to the heavy-hole effective mass along the [001] direction.

To implement this idea, we add and subtract a term $\hbar^2/2m^+(\hat{k}_x^2+\hat{k}_y^2)$ to $\hat{P}_1$, and a term $\hbar^2/2m^-(\hat{k}_x^2+\hat{k}_y^2)$ to $\hat{P}_2$. Then we obtain

$$\hat{P}^+=\hat{P}_1=\frac{1}{m^+}(\hat{k}_x^2+\hat{k}_y^2)+p_x^+\hat{k}_x^2+p_y^+\hat{k}_y^2 + \left(\gamma_1-\frac{\gamma_2-3\gamma_3}{2}\right)k_z^2, \tag{12a}$$

$$\hat{P}^-=\hat{P}_2=\frac{1}{m^-}(\hat{k}_x^2+\hat{k}_y^2)+p_x^-\hat{k}_x^2+p_y^-\hat{k}_y^2 + \left(\gamma_1+\frac{\gamma_2-3\gamma_3}{2}\right)k_z^2, \tag{12b}$$

where

$$p_x^+=\left(\gamma_1-\frac{\gamma_2+3\gamma_3}{2}\right)-\frac{1}{m^+}, \tag{13a}$$

$$p_y^+=(\gamma_1+\gamma_2)-\frac{1}{m^+}, \tag{13b}$$

$$p_x^-=\left(\gamma_1+\frac{\gamma_2+3\gamma_3}{2}\right)-\frac{1}{m^-}, \tag{13c}$$

$$p_y^-=(\gamma_1-\gamma_2)-\frac{1}{m^-}. \tag{13d}$$

Then we solve the equations (11a) and (11b) by a plane-wave expansion, as outlined in Ref. 22. Typically, we fix two energy cutoffs, $E_{\rm cut}^+$ and $E_{\rm cut}^-$, and we find the N^+ and N^- eigenstates which fall below the cutoffs. Using the eigenfunctions ϕ_ν^+, ϕ_μ^-, we form the following basis set:

$$|+,\nu,\uparrow\rangle=\begin{pmatrix}\phi_\nu^+\\0\\0\\0\end{pmatrix},\quad |+,\nu,\downarrow\rangle=\begin{pmatrix}0\\0\\0\\\phi_\nu^+\end{pmatrix}, \tag{14a}$$

$$|-,\mu,\uparrow\rangle=\begin{pmatrix}0\\\phi_\mu^-\\0\\0\end{pmatrix},\quad |-,\mu,\downarrow\rangle=\begin{pmatrix}0\\0\\\phi_\mu^-\\0\end{pmatrix}, \tag{14b}$$

with $\nu=1\ldots N^+$ and $\mu=1\ldots N^-$, and we expand ψ_α^h in this basis:

$$\psi_\alpha^h=\sum_{\nu\sigma}C_\alpha^+(\nu,\sigma)|+,\nu,\sigma\rangle+\sum_{\mu\sigma}C_\alpha^-(\mu,\sigma)|-,\mu,\sigma\rangle. \tag{15}$$

The explicit matrix elements of $\hat{\mathbf{H}}_L$ in this basis are given in Appendix B. The total dimension of the Hamiltonian matrix in this representation is $2\times(N^++N^-)$. All we need to compute, in order to evaluate the matrix elements, are integrals of the kind

$$\int_\Omega[\phi_i^\gamma(x,y)]^*\hat{k}_\beta\phi_j^{\gamma'}(x,y)dx\,dy, \tag{16a}$$

$$\int_\Omega[\phi_i^\gamma(x,y)]^*\hat{k}_\beta\hat{k}_{\beta'}\phi_j^{\gamma'}(x,y)dx\,dy, \tag{16b}$$

evaluated over the supercell volume Ω, where $\beta,\beta'\in\{x,y\}$ and $\gamma,\gamma'\in\{+,-\}$; these are easily obtained given the plane-wave expansions of the ϕ_i^+'s and ϕ_i^-'s. The choice of m^+, m^-, which is important in order to obtain an efficient convergence, is discussed in detail in Appendix A; here we only anticipate that in all our calculations we use $m^+=m^-=(\gamma_1-2\gamma_2)^{-1}$.

Once we have calculated the electron and hole subbands by the above method, we are in the position to evaluate the absorption spectrum $\alpha_\epsilon(\hbar\omega)$ in the dipole approximation, summing the dipole matrix element, with the appropriate polarization of light ϵ, over all electron and hole states:

$$\alpha_\epsilon(\hbar\omega)\propto\sum_{\alpha,n,\sigma}|M_{\alpha\to n,\sigma}^\epsilon|^2\delta(E_n^e+E_\alpha^h+E_g-\hbar\omega), \tag{17}$$

where the optical matrix elements $M_{\alpha\to n,\sigma}^\epsilon$ are given in Appendix C, and E_g is the bulk energy gap of GaAs; typically, a set of sixty k_z points have been included in the summation. The absorption spectra shown in this paper have been obtained by superimposing a Gaussian broadening σ_b to

TABLE II. *V*-QWR's sample parameters.

	A/SL	*A*/AlAs	*B*/SL	*B*/AlAs
L (nm)	8.7	8.7	6.83	6.83
Barrier type	$(AlAs)_4/(GaAs)_8$	AlAs	$(AlAs)_4/(GaAs)_8$	AlAs
$V^e_{\rm eff}$ (eV)	0.150	1.036	0.150	1.036
$V^h_{\rm eff}$ (eV)	0.085	0.558	0.085	0.558

$\alpha_\epsilon(\hbar\omega)$, in order to simulate the inhomogeneous broadening due to structural imperfections of the samples. The broadened spectrum is obtained as

$$\alpha_\epsilon(\hbar\omega)=\int_{-\infty}^{\infty}\alpha_\epsilon(\hbar\omega')e^{-\hbar^2(\omega-\omega')^2/2\sigma_b^2}d\omega'. \qquad (18)$$

II. BAND STRUCTURE AND OPTICAL PROPERTIES OF *V*-SHAPED WIRES

A. Samples

As a prototype of *V*-QWR's, we first consider a sample described in Refs. 5, 27. This consists of an active GaAs layer embedded in a $(AlAs)_4/(GaAs)_8$ SL, overgrown by molecular beam epitaxy on the exposed surface of the etched substrate. As in Refs. 23, 27, we use the *V*-shaped potential profile obtained by digitalizing a TEM micrograph of the sample. We also adopt the same supercell geometry as in Refs. 23, 27. The complicated structure of the SL which provides the quasi-one-dimensional confinement is modeled by a homogeneous barrier with effective conduction- and valence-band offsets, $V^e_{\rm eff}$ and $V^h_{\rm eff}$, respectively. Based on previous investigations[27,23] for the same sample, we take $V^e_{\rm eff}=150$ meV and $V^h_{\rm eff}=85$ meV. It should be noted that the effort of including exactly the confining SL in the calculations would not necessarily result in improved accuracy, as the envelope-function approximation itself loses its validity for such short-period SL's.

In order to investigate the role of the confinement in the optical properties, we shall consider two sample profiles, which differ in the value of the confinement length L at the bottom of the *V*-shaped region (see Fig. 1): profile *A* ($L=8.7$ nm) and profile *B* ($L=6.83$ nm). These SL-embedded QWR's will be labeled *A*/SL and *B*/SL.

A key issue which makes nm-scale QWR's interesting for electro-optical applications are large confinement energies which can be obtained with large band offsets in addition to geometric confinement. In view of this fact, we shall compare the samples described above with samples having the same profiles and barriers constituted by pure AlAs, that we will label *A*/AlAs and *B*/AlAs. The parameters of the four samples are summarized in Table II.

B. Band structure

A qualitative interpretation of the band structure of a *V*-QWR can be obtained by adding to a QW of width L an additional lateral confinement due to the crescent shape of the profile. In the lowest approximation, the latter can be thought of as a parabolic potential[1] which splits each subband of the parent QW into a new set of subbands. Since the additional confinement is less effective than the confinement due to the original QW, the new sets of subbands have smaller gaps with respect to the subband splittings of the parent QW. This simplified picture will serve as a guideline for the discussion of numerical results obtained for the actual samples.

TABLE III. Confinement energies (in meV) of the lowest conduction and valence states at $k_z=0$ for the *V*-QWR's. Note that at $k_z=0$ spin degeneracy holds. Therefore, subband $m=1$ is degenerate to $m=2$, etc. (Ref. 24).

	Electrons			
n	*A*/SL	*A*/AlAs	*B*/SL	*B*/AlAs
1	43.3	68.3	55.5	98.8
2	57.3	91.9	63.2	117.0
3	65.3	112.5	67.0	124.0
4	69.8	126.1	72.4	132.2
	Holes			
m	*A*/SL	*A*/AlAs	*B*/SL	*B*/AlAs
1,2	10.7	14.4	13.1	18.7
3,4	13.1	18.1	13.8	19.5
5,6	14.4	20.0	15.6	21.7
7,8	15.8	21.8	17.1	23.7

The calculated energies at $k_z=0$ of the lowest conduction and valence states are listed for reference in Table III for the four samples. In the following we shall focus on hole subbands, which are shown in Fig. 2 (right panel) for sample *A*/SL. First, we note that at $k_z=0$ each subband is doubly degenerate, while at finite k_z the subbands are spin split, due to the lack of inversion symmetry of the confining potential.[28] Splittings are in the range of few meV. Second, a strongly nonparabolic energy dispersion is evident. This fact, familiar from QW's, is due to mixing of states with HH ($J_m=\pm 3/2$) character and LH ($J_m=\pm 1/2$) character.

The HH/LH character of hole states influences the optical properties of the sample, since different atomic orbital components have different oscillator strengths; of particular interest from this point of view are the $k_z=0$ states which, due to the large density of states (DOS) stemming from their quasi-one-dimensional character, mainly contribute to the

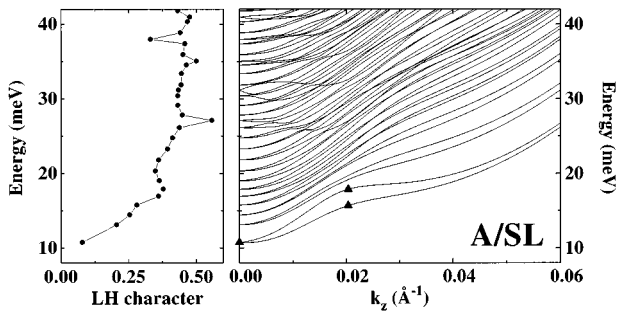

FIG. 2. Right panel: hole band structure along the free axis $[\bar{1}10]$ of the *V*-QWR labeled *A*/SL. Black triangles indicate the eigenvalues used in the later Fig. 11 to analyze the convergence. Left panel: LH character of the $k_z=0$ states; the **J** quantization axis is taken along [001].

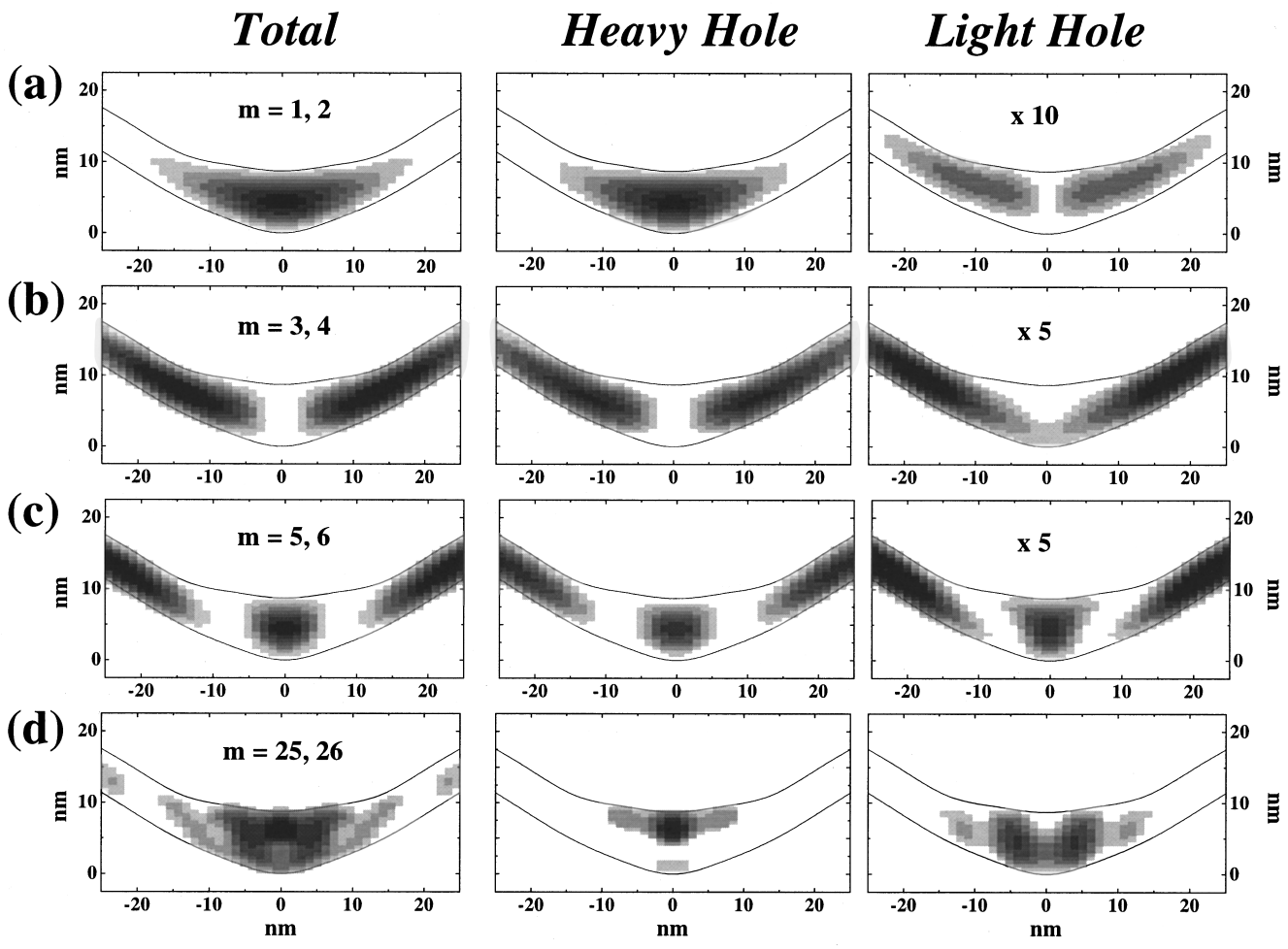

FIG. 3. Total charge density (left panels), and HH- and LH-projected charge densities (center and right panels) of selected hole subbands, according to the labels, at $k_z=0$ for the same *V*-QWR of Fig. 2. Full lines indicate the GaAs/SL interfaces. For clarity, some charge density maps have been magnified by a factor of 5 or 10, as indicated by labels. Note that the hole subbands $m=1,3,5,\ldots$ at $k_z=0$ are degenerate with the subbands $m=2,4,6,\ldots$, (Ref. 24) and the total and projected charge densities are equal for degenerate states.

absorption intensity. Contrary to the case of QW's, hole subbands cannot be strictly classified as HH and LH states even at $k_z=0$. To define the HH/LH character in the present samples, we note that the direction of strongest confinement is the [001] direction, as demonstrated by charge density maps of the lowest-lying states which we will show later in Fig. 3. It is therefore meaningful to calculate the HH/LH character along this direction, because this would be the quantization axis of J in an equivalent [001]-grown QW of width L. To do this, we calculate the rotated vector $\boldsymbol{\psi}^h_{\alpha,R}(x,y)=\mathbf{R}^{-1}\cdot\boldsymbol{\psi}^h_{\alpha}(x,y)$, where

$$\mathbf{R}=\frac{1}{2\sqrt{2}}\begin{pmatrix}1 & -\sqrt{3} & \sqrt{3} & 1\\ \sqrt{3} & 1 & -1 & \sqrt{3}\\ \sqrt{3} & 1 & 1 & -\sqrt{3}\\ 1 & -\sqrt{3} & -\sqrt{3} & -1\end{pmatrix}. \tag{19}$$

$\mathbf{R}$ is obtained by diagonalizing the matrix $\mathbf{J}_y$ written in the representation in which $\mathbf{J}_x$ is diagonal, with eigenvalues J_m. Then we define the HH- and LH-projected charge densities

$$\rho^{\mathrm{HH}}_{\alpha}(x,y)=\sum_{J_m=\pm 3/2}|\psi^h_{\alpha,R,J_m}(x,y)|^2, \tag{20a}$$

$$\rho^{\mathrm{LH}}_{\alpha}(x,y)=\sum_{J_m=\pm 1/2}|\psi^h_{\alpha,R,J_m}(x,y)|^2. \tag{20b}$$

Finally, the HH and LH character is obtained by integrating the above charge densities over all space. (In the above equations, the real-space representation is chosen for clarity. The corresponding expressions in Fourier space, which we use in the numerical implementation, are very easy to obtain and are not explicitated here.)

In the left panel of Fig. 2 we show the calculated LH character of the hole subbands at $k_z=0$. This is best analyzed in connection with Fig. 3, where we show the total and projected charge densities of the hole states at $k_z=0$ for the same *A*/SL sample. In the ground state, the LH component is rather small ($\sim 8\%$), but it increases rapidly for the excited subbands. Correspondingly, the ground state is well localized [Fig. 3(a)], while the lowest excited states [Figs. 3(b), 3(c)] have wave functions which increasingly extend along the *V*-QWR sidewalls. The regular increase of the LH compo-

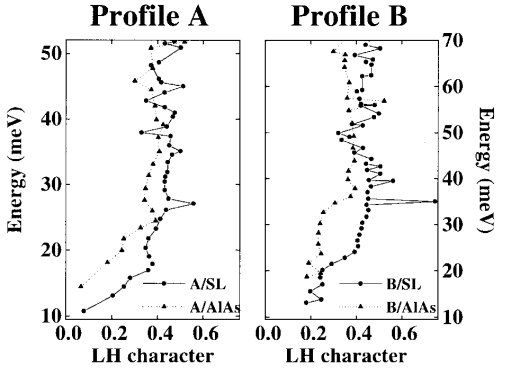

FIG. 4. LH character vs subband energy at $k_z=0$ for samples with profile A (left panel) and B (right panel), and with SL or AlAs barriers (full circles and triangles, respectively).

nent is interrupted by the $m=25,\ 26$ levels (13th doublet: recall that each point at $k_z=0$ is doubly degenerate) at ~ 27 meV which is mainly of LH character (56%). This can be interpreted as the reminiscent of the LH state of a QW with confinement length L. The wave function of this level [Fig. 3(d)], in fact, is again well localized, analogously to the ground state, and in contrast to the wave functions of nearby states. We shall comment later on the fingerprints of this strongly LH-like state in the optical spectra, and, particularly, in the optical anisotropy. Note also that in Fig. 2 there are other ''jumps'' in the LH character at higher energies; these correspond to energies where ladders of levels of different symmetries, like an additional nodal plane parallel to the [110] direction, begin.

In Fig. 4 we compare the LH character vs subband energy at $k_z=0$ for samples with different barriers (SL and pure AlAs). For both profiles A and B, the strong confinement due to AlAs barriers induces not only the expected blueshift of the subbands, but also reduces the LH character of the lowest LH-like state, as compared to SL barriers: in sample A/SL, the $m=25,\ 26$ doublet is 56% LH, while its counterpart in sample A/AlAs, the $m=27,\ 28$ doublet, is only 42% LH. In sample B/SL, the $m=35,\ 36$ doublet is 75% LH, while its counterpart in sample B/AlAs, the $m=37,\ 38$ doublet, is only 52% LH.

C. Optical properties

In Fig. 5 we show the calculated absorption intensity for the four samples of Table II and for light linearly polarized parallel to the wire axis, $I_{\|}$, and perpendicular to it along the [110] direction, $I_{\perp}$. A Gaussian broadening of $\sigma_b=\pm 4.5$ meV has been included.[23] For all samples, we also report the relative optical anisotropy (thick lines in Fig. 5), defined as $100*(I_{\|}-I_{\perp})/I_{\|}$. The optical absorption spectra are obtained integrating over the whole band structure (i.e., integrating over k_z and summing over electron and hole subbands and spin); however, for illustration we show the strongest optical transitions due to $k_z=0$ states, and for one spin orientation of the conduction electrons, for light polarization perpendicular to the QWR axis (histograms in Fig. 5). To identify the electron and hole states involved in each transition, we use the label n/m, where n and m are, respectively, the indices of the conduction and valence states.

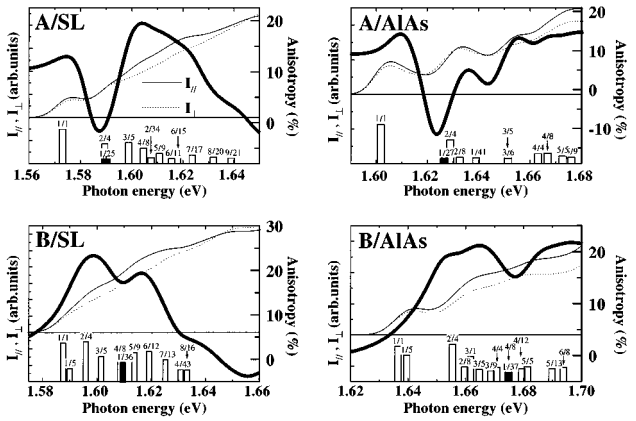

FIG. 5. Optical absorption intensity for linearly polarized light parallel (thin solid lines) and perpendicular (thin dotted lines) to the wire axis for the four samples listed in Table II. The relative anisotropy is also shown (thick lines) in the scale on the right-hand side of each panel. A Gaussian broadening of $\sigma_b=\pm 4.5$ meV is included. For each sample, we show a histogram of the strongest optical transitions at $k_z=0$ and for one spin orientation, for light polarizion perpendicular the QWR axis. Each bar is proportional in height to the oscillator strength, and it is labeled with n/m, where n is the index of the conduction state and m the index of the valence state involved in the transition (Ref. 24).

We first focus on sample A/SL, for which experimental data are available.[23] The calculated anisotropy in the low-energy part ($\lesssim 1.62$ eV) is 10–20 %, with a deep minimum at ~ 1.59 eV, where the anisotropy is almost suppressed. Both the average anisotropy and the position of the minimum are in *quantitative* agreement with experimental data.[23] The agreement worsens at higher energies ($\gtrsim 1.62$ eV), where the calculated anisotropy drops rapidly and finally changes sign, while experimental data[23] show an increase. We believe that this discrepancy is due to our ''effective'' description of the barriers which affects particularly the higher-lying hole states.

By comparing the calculated anisotropy of the four samples, it appears that a more or less pronounced dip over a range of ~ 10 meV (i.e., the linewidth of the broadened spectra) is always present in the low-energy range of the spectrum, superimposed onto a background of an otherwise large and positive anisotropy. Additional structure, particularly for sample A/AlAs, is also present in the high-energy range. Note also that the maximum anisotropy is in the range 15–25 %, and does not change dramatically in the different samples.

By studying the optical matrix elements, it can be shown that the dips in the anisotropy are due to states with a large LH character,[17] e.g., the $m=25$ subband in sample A/SL. Since this is a localized state and has a large spatial overlap with the first conduction subband, it contributes to the low-energy part of the spectrum. This is true, in general: as can be seen from Fig. 5, for all samples the anisotropy dip corresponds to a $k_z=0$ transition (highlighted as black bars in the histograms) between the electron ground state ($n=1$) and an excited hole state which is the $m=25$, the $m=27$, the $m=36$, and the $m=37$ level for A/SL, A/AlAs, B/SL, and B/AlAs, respectively. For sample A/SL, comparison with

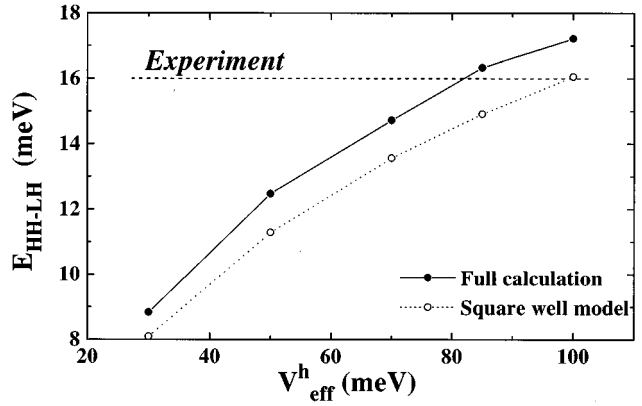

FIG. 6. Energy gap between the hole ground state and the first localized state with a strong LH character for the *V*-QWR sample labeled *A*/SL as a function of the effective valence-band offset $V^h_{\rm eff}$. Full dots: full calculation. Empty dots: square well model for a QW of width L and barrier height $V^h_{\rm eff}$, the HH and LH levels are obtained with $m_{\rm HH}=0.377$ and $m_{\rm LH}=0.090$, respectively. The experimental value is obtained as explained in the text.

Fig. 2 shows that the involved $m=25$ hole state has a strong LH character and its wave function [Fig. 3(d)] is strongly localized. The large LH component assumes that the intensity for the two polarizations is reversed with respect to the strongly HH-like ground state, causing the dip in the anisotropy at 1.59 meV. A similar correspondence between the dip and a localized LH-like state applies also to the other samples.

An immediate consequence of the above result is that, since both the ground HH state and the LH-like state couple with the lowest electron subband, *the difference in energy between the onset of the continuum and the position of the dip in the anisotropy is a direct measure of the energy splitting between the ground HH and the first LH state, independently of the electron confinement.* Note that such information cannot be extracted from the absorption spectra alone, as the large broadening prevents the identification of any single transition apart from the fundamental one.

The HH/LH splitting obtained in the above manner can be used to extract band structure parameters as, for example, the effective hole confinement $V^h_{\rm eff}$. In the measured PLE spectra for sample *A*/SL,[23] the anisotropy dip lies ~ 16 meV above the onset of the continuum; in Fig. 6 we report the HH/LH splitting calculated for several values of $V^h_{\rm eff}$ (full dots) for this sample. We also show, for comparison, the HH/LH splitting calculated by a simple square well model for a QW of width L (empty dots), using the bulk HH and LH effective mass along [001] . It can be seen that the splitting is quite sensitive to $V^h_{\rm eff}$, and that the experimental value is compatible with $V^h_{\rm eff}\sim 80$ meV. This observation provides a good criterion for choosing the confinement energy of holes, which would otherwise be rather arbitrary. Using this procedure, $V^h_{\rm eff}$ was finally taken equal to 85 meV in Ref. 23. Note that a variation of the valence-band offset of ± 15 meV shifts the HH/LH splitting of ± 1.3 meV, well within the experimental accuracy for the determination of the HH/LH splitting.[23] Note also that, for a rough estimation of $V^h_{\rm eff}$, calculations using a simple square well model may be sufficient.

The comparison with the absorption spectra demonstrates that $k_z=0$ transitions alone give a poor estimate of the integrated spectrum. This is due to the DOS contribution of the hole subbands which are strongly nonparabolic, and have a large DOS also for k_z points away from $k_z=0$ (see Fig. 2). Finally, note the relaxation of selection rules for $k_z=0$ transitions shown in Fig. 5. Indeed, if the envelope-function parity-conserving selection rule would be obeyed, only transitions of the type $n/(m=2n)$ or $n/(m=2n-1)$ (depending on electron spin orientation) would be allowed.

III. BAND STRUCTURE AND OPTICAL PROPERTIES OF *T*-SHAPED WIRES

A. Samples

We investigate a *T*-QWR with the geometry sketched in Fig. 1. In our calculation, the SL grown along the [001] direction is constituted by 5.3 nm wide QW's (QW1), separated from each other by 50 nm wide AlAs barriers, while the QW grown along the [110] direction (QW2) is 4.8 nm wide. These parameters correspond to a sample for which polarization-dependent PLE spectra are available.[12]

Note that the *T*-QWR's which form at the intersection between QW1 and QW2 are not uncoupled in the [001] direction, due to the SL structure of QW1's, a fact which we fully take into account in the supercell representation used in our calculations. On the other hand, the *T*-QWR's are isolated along the [110] direction; in our calculations, this is simulated by truncating QW1 with a AlAs barrier 50 nm on the left-hand side.

B. Band structure

The nature of the 1D confinement in *T*-QWR's is rather different with respect to the *V*-QWR's case. There, we used the picture of a lateral confinement added on a QW structure which, therefore, localizes all states in the x-y plane. Conversely, *T*-QWR states can be better interpreted as the result of the coupling between 2D states of the QW's, QW1, and QW2. Beside perturbing the 2D states, this coupling also induces localized states or resonances; these can be also seen as due to a 1D defect in the otherwise translationally invariant (in the QW plane) 2D states of a QW, due to the coupling with the other QW. This picture has nontrivial consequences, particularly for hole states, which we analyze in the following.

First, we focus on the lowest-lying states at $k_z=0$. Electrons and holes are very different from this point of view: contrary to the electron effective mass which is isotropic in GaAs, the HH effective mass is strongly anisotropic between the [001] direction ($m_{\rm HH}=0.377$) and the [110] direction ($m_{\rm HH}=0.69$). The effect of this difference is shown in Fig. 7, where we report the total charge densities for the lowest electron and hole states at $k_z=0$. For the present structure, being QW1 and QW2 of comparable width, the electron ground state [Fig. 7(a)] is a quasi-one-dimensional state extending both in QW1 and QW2; the lowest excited subbands [Figs. 7(b), (c), (d)] belong to the continuum of 2D states of QW1, since QW1 is wider (actually, discrete levels are obtained here, due to the supercell method); the localized quasi-one-dimensional electron lies 15 meV below the QW1 continuum.

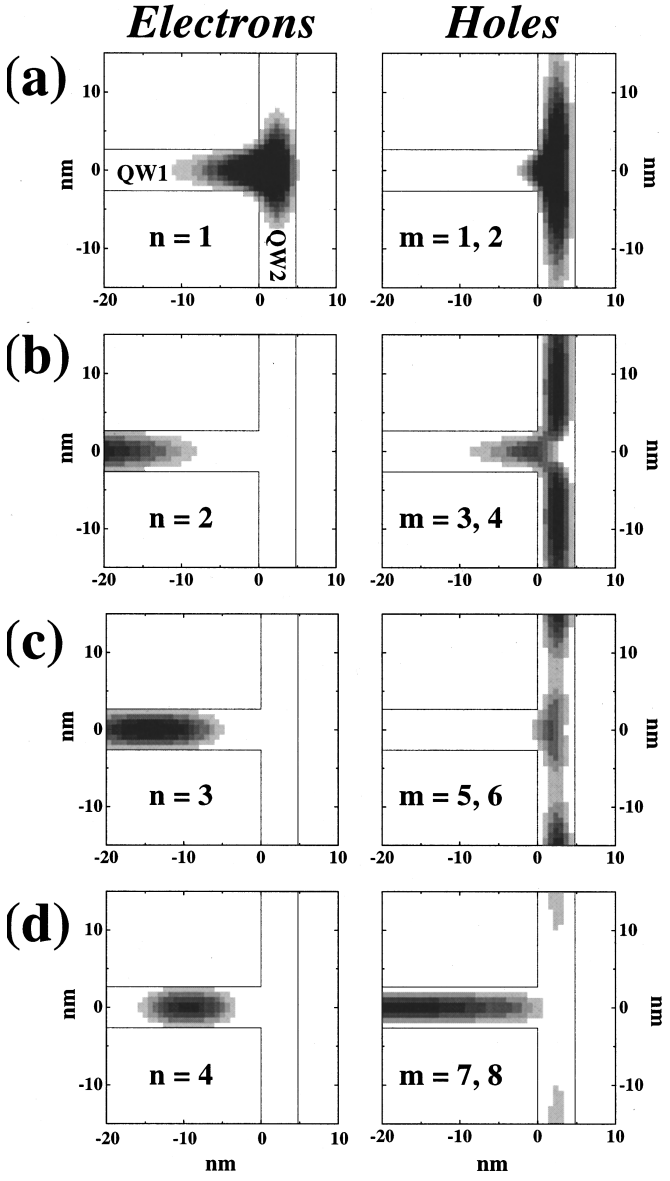

FIG. 7. Total charge density of electrons (left panels) and holes (right panels) of the lowest $k_z=0$ subbands for the T-QWR.

On the contrary, for holes the larger mass along [110] more than compensate for the smaller width of QW2, and the hole ground state [Fig. 7(a)], although localized in the center of the T, is much more a QW2-like state, only weakly perturbed by coupling to QW1; accordingly, the lowest excited hole subbands [Fig. 7(b), (c)] are basically 2D states belonging to QW2, up to the fourth level [Fig. 7(d)], which is a QW1 state. The quasi-one-dimensional ground state is practically degenerate with the QW2 continuum; note, however, that in contrast to conduction electrons, there is a second hole level [Fig. 7(b)] with a significant component along QW1.

The full band structure of holes is shown in the right-hand panel of Fig. 8. In the rather complex dispersion of the subbands, we can distinguish a peculiar feature of T-QWR, namely, a huge spin splitting of the lowest doublet at finite k_z which, at $k_z \simeq 0.035$ Å^{-1}, is ~ 15 meV for the present structure.

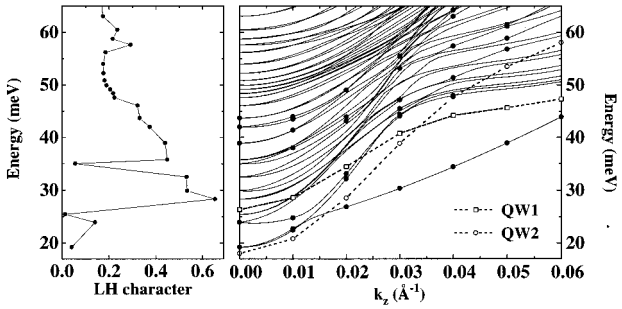

FIG. 8. Right panel: hole band structure along the free axis $[\bar{1}10]$ of the T-QWR. Solid lines show the dispersion of all states resulting from the full calculation for our supercell geometry. The full circles identify the states that, from direct inspection of the wave function, exhibit a predominantly localized character at center of the T, and are therefore assigned to quasi-one-dimensional QWR-like states or resonances. As explained in the text, the remaining states are similar to 2D QW-like states, with the charge density localized mostly in QW1 or QW2. Open squares and circles show the lowest-hole subbands of the parent isolated QW1 and QW2, respectively. Left panel: LH character (with **J** quantization axis along [110]) of the $k_z=0$ states.

Before discussing the origin of such a large spin splitting, it is useful to examine the actual localization of the calculated states in the QWR. To this aim, we need to discriminate the states peaked around the center of the T from states that are typical of one of the parent QW's and are left essentially unchanged by the interaction with the other one. This is particularly useful because we expect that most of the states of Fig. 8 simply arise from folding of QW states induced by the supercell periodicity and to the truncation of the T along the [110] direction. Therefore, in Fig. 8 we identify by full circles those states which, by direct inspection of the wave function, show a strong localization in the center of the T. Indeed, it appears that only a limited subset has predominantly a localized character, and can therefore be assigned to quasi-one-dimensional QWR-like states or resonances. These include the localized states arising from the lowest two doublets, already discussed above, as well as the resonant states falling around 40 meV. The remaining states are similar to 2D QW-like states, with the charge density localized mostly in QW1 or QW2.

To clarify the origin of the large spin splitting, it is useful to compare the band structure of the T-QWR with the hole subbands of the parent isolated QW1 and QW2. In Fig. 8 we show with open squares and open circles the lowest HH subband of QW1 and QW2; the LH subbands, for these thicknesses, lie high in energy (>80 meV in QW1 and >100 meV in QW2).[29] A small gap of ~ 8 meV separates the two levels at $k_z=0$; as already noted above, the lowest state is QW2, due to the larger HH mass. Owing to different HH-LH mixing in each QW separately, the HH subbands of the two parent QW's have different energy dispersion as a function of k_z and cross at some finite k_z.

Large spin splittings are, in general, an effect of HH-LH mixing in asymmetric structures.[30] In the present case, however, the energy difference between the HH and LH levels in each isolated QW is too large to explain the huge splitting that we have found in the lowest-energy subbands of the

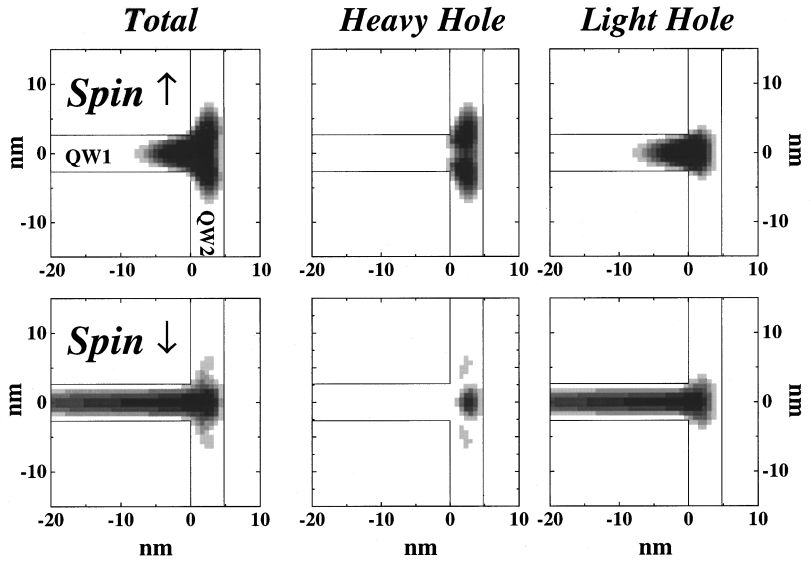

FIG. 9. Total charge density of the lowest two hole states of the *T*-QWR at $k_z = 0.035$ Å^{-1}. The HH- and LH-projected charge densities of each state are also shown separately in the center and right-hand panels. Full lines indicate the GaAs/AlAs interfaces.

QWR. Naively, one would rather expect small gaps (induced only indirectly by coupling to the far-lying LH states) to open at the crossing of the QW1 and QW2 subbands. Note, however, that the HH states of the parent QW's are eigenstates of **J** with $J_m = \pm 3/2$, but *with the quantization axis along different directions*. Taking, for example, the **J** quantization axis along [110], a HH state of QW2 is $|\mathrm{QW2}\rangle = |3/2, +3/2\rangle$ (for one of the degenerate spin orientations). A HH state of QW1 *written in the same basis*, is

$$|\mathrm{QW1}\rangle = \frac{1}{2\sqrt{2}}(|3/2,+3/2\rangle + \sqrt{3}|3/2,+1/2\rangle + \sqrt{3}|3/2,-1/2\rangle + |3/2,-3/2\rangle). \quad (21)$$

In words, a HH state of QW1 has a strong LH component from the point of view of QW2. Therefore, the lowest HH subbands arising from QW1 and QW2 are strongly coupled, which results in a strong avoided-crossing behavior and a very large spin splitting.

This interpretation is supported by our calculation of the LH character, which is shown in the left panel of Fig. 8. In view of the fact that the hole ground state is rather QW2-like, we have computed the LH character with the quantization axis along [110], i.e., it is obtained, as in Sec. II, by integrating the projected charge densities [see Eqs. (20a)–(20b)], but using the ψ^h_α instead of the rotated $\psi^h_{\alpha,R}$. As expected, the lowest subbands are nearly pure HH, being localized in QW2 (see Fig. 7), while the $m = 7,8$ subbands are more than 60% LH. This should not be interpreted as a mixing with LH states of QW2; rather, it is a manifestation of the fact that this state is localized in QW1 and, therefore, does not have a well-defined orbital character along [110].

We conclude our analysis of the lowest spin-split doublet by noting that, as k_z increases, only the lowest level remains a well localized, quasi-one-dimensional state, while its spin companion gradually merges into the QW1 quasicontinuum (at large wave vectors, QW1 becomes the ground state). For illustration, we show in Fig. 9 the charge density of the two lowest levels at $k_z = 0.035$ Å^{-1} (close to the wave vector where the QW2 and QW1 dispersions cross). The lowest state (labeled ↑), which falls far in energy from the QW bands, is strongly localized at the intersection of the QW's. The higher state (labeled ↑) is peaked at the center of the *T* but it also extends quite far into QW1.

C. Optical properties

In Fig. 10 we show the calculated absorption intensity for the *T*-QWR and for light linearly polarized parallel to the wire axis, $I_\parallel$, and perpendicular to it along the [001] direction, $I_\perp$. A Gaussian broadening of $\sigma_b = \pm 5$ meV has been included. We can identify four main structures, a peak around 1.65 eV, another peak around 1.68 eV (with a minor shoulder on the low-energy side), a large composite structure beginning above 1.7 eV, and another large structure at 1.74 eV. Of these, only the lowest peak involves essentially pure QWR-like localized states [Fig. 7(a)]. The second structure involves transitions from the next electron state, extending in QW1 [see Fig. 7(b)], to the first hole states with significant spatial overlap [see Fig. 7(d)]. The structure above 1.7 meV

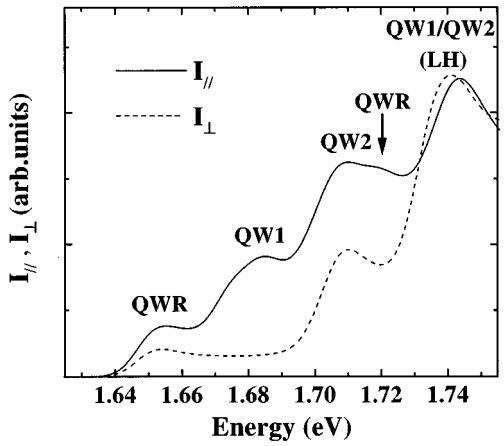

FIG. 10. Absorption intensity of the *T*-QWR for light linearly polarized parallel (solid line) and perpendicular (dashed line) to the wire axis along [001], labeled with the main contributions to the peak intensities. A Gaussian broadening of ±5 meV is included.

involves predominantly QW2 states, with a contribution from higher QWR resonances which produce the high-energy shoulder in $I_{\|}$. Finally, the large peak at 1.74 eV is due to many subbands, with a significant contribution from LH states belonging to both QW's. The lowest three structures are polarization dependent with $I_{\|} > I_{\perp}$. The anisotropy is maximum for the second structure, for which $I_{\perp}$ is very small, consistently with the expectation for a (001) QW. The higher structure, on the other hand, is nearly polarization independent, due to the LH contributions.

These results can be compared with the experimental PLE spectra of Ref. 12. There, three main structures occur at 1.64, around 1.67–1.68, and above 1.7 meV. The agreement with the calculated spectra is again surprisingly good, taking into account that these neglect excitonic effects. The experimental assignment of the first structure to a QWR-like state and the successive structures to QW1-like states, based on the comparison with reference QW's, is fully consistent with our picture. As concerns intensities, the agreement is also reasonably good if one considers that the weight of the QWR peak is sensitive to the relative volume occupied by the QW's, which enters the calculation through the choice of the supercell. On the other hand, the reasons of an enhanced intensity of QW1-like features in the PLE experimental data are discussed in Ref. 12. Finally, we compare our results with the observed values of the anisotropy.[12] From PLE, Akiyama *et al.* estimate $I_{\perp} = 0.39 I_{\|}$ for the QWR peak, and $I_{\perp} = 0.14 I_{\|}$ for the next structure assigned to QW1. The corresponding theoretical values from Fig. 10 are approximately $I_{\perp} = 0.52 I_{\|}$ and $I_{\perp} = 0.19 I_{\|}$ (the coefficients are slightly larger, 0.57 and 0.17, respectively, if the broadening is reduced to $\sigma_b = \pm 1.5$ meV). The very different anisotropy of the two structures is therefore in qualitative agreement with experiments, although further investigation would be required to understand the origin of the difference.

SUMMARY AND CONCLUSIONS

We have presented an accurate and efficient approach that allows us to calculate the electronic and optical properties of quantum wires, taking into account valence-band mixing effects together with realistic profiles of the confining potentials. We have studied specifically *V*- and *T*-shaped quantum wires, where the shape of the confinement region differs considerably from the model geometries assumed in most of the previous investigations. The two classes of wires differ significantly in the structure of their energy spectra: while the crescent shape of *V*-QWR's induces a series of localized quasi-one-dimensional levels, only the lowest states of *T*-QWR's are clearly localized in the wire because of the subsequent onset of the continua of the parent QW's. The consequences on the optical spectra have been discussed in detail. In particular, we have focused on the optical anisotropy, and demonstrated that the analysis of anisotropy spectra can be used as an effective tool to extract information on valence states, usually very difficult to obtain otherwise.

Comparison with very recent PLE spectra for both classes of wires shows good agreement, in spite of our neglecting excitonic effects. As we discussed in the Introduction, this agreement might be due to the symmetry properties of the Coulomb interaction and, therefore, might be a rather general feature. However, while the approximation of neglecting excitonic effects is very convenient from the computational point of view, its accuracy for a given class of materials should be established *a posteriori* from comparison to experiments, as we have positively tested in this paper for *V*-QWR's and *T*-QWR's.

As a final remark, we stress that all our calculations have been performed by a numerical method which proved computationally very convenient. Furthermore, our method lends itself to include calculations of Coulomb correlation effects on the linear and nonlinear optical properties of these wires which are currently implemented only for noninteracting valence bands,[22] as well as to include external magnetic fields[20,31] to interpret magnetoluminescence experiments.

ACKNOWLEDGMENTS

This work was supported in part by the EC Commission through the HCM Network ''ULTRAFAST.''

APPENDIX A: BASIS SET CONVERGENCE AND THE CHOICE OF m^+, m^-

The fictitious masses m^+, m^- entering Eqs. (11a) and (11b) can be chosen arbitrarily. In this appendix we will show that a judicious choice can lead to a significant improvement in the basis set convergence and the lowering of the computational cost of the calculation. Note that the convergence with respect to the number of functions ϕ_ν^+, ϕ_ν^- included in the basis set, which we investigate below, is a separate problem from the convergence in the plane-wave expansion of the ϕ_ν^+, ϕ_ν^- themselves which, for a given structure, must therefore be checked once and for all *before* the diagonalization of the Luttinger Hamiltonian is started.

In Fig. 11 we show the behavior of the lowest hole eigenvalues as a function of the number of basis functions $N^+ + N^-$. The calculations have been performed for the *V*-QWR *A*/SL, which is described in detail in Sec. II. The eigenvalues reported in Fig. 11 are highlighted by black triangles in the full band structure of the same *V*-QWR shown in Fig. 2: they are the doubly degenerate lowest eigenvalue at $k_z = 0$ [panel (a)], and the two spin-split lowest eigenvalues at $k_z = 0.02$ Å^{-1} [panels (b) and (c)].

In each panel of Fig. 11 we show two sets of calculations, both obtained with $m^+ = (\gamma_1 - 2\gamma_2)^{-1}$, but with different choices of m^-. The empty dots are obtained with $m^- = (\gamma_1 + 2\gamma_2)^{-1}$. With this choice, m^+ and m^- are the HH and LH effective masses along the [001] crystallographic direction; since this is the direction of strongest confinement for these *V*-QWR's (see next section), these are the ''physical'' masses in the sense that, for example, they would determine the HH and LH levels of a QW with comparable confinement length grown in this direction. It can be noted, however, that convergence is achieved only within ~ 1 meV with $N^+ + N^-$ as high as 280, which corresponds to $E_{\rm cut}^+ = 120$ meV and $E_{\rm cut}^- = 200$ meV; these, in turn, should be compared with the low barrier height of this sample, which is 85 meV. Therefore, one needs to reach energies high in the continuum to achieve convergence. The couples of empty dots at $N^+ + N^- = 210$ are obtained with

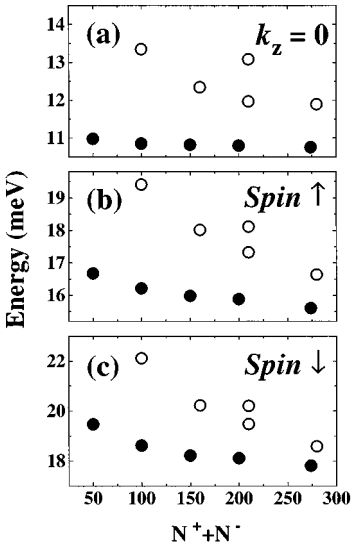

FIG. 11. Energy of the lowest eigenvalues for the *V*-QWR labeled *A*/SL (see Sec. II) at (a) $k_z=0$ (spin degenerate) and (b), (c) at $k_z=0.02$ Å^{-1} for the two spin-split states. Empty dots: eigenvalues calculated with $m^+=(\gamma_1-2\gamma_2)^{-1}$, $m^-=(\gamma_1+2\gamma_2)^{-1}$. Black dots: eigenvalues calculated with $m^+=m^-=(\gamma_1-2\gamma_2)^{-1}$. The pairs of empty dots at $N^++N^-=210$ are calculated with $(N^+,\ N^-)=(125,\ 85)$ (upper dots) and $(N^+,\ N^-)=(97,\ 113)$ (lower dots).

two different choices of the pair $(N^+,\ N^-)$: (125, 85) for the upper points, and (97, 113) for the lower points. We conclude that, with fixed N^++N^-, the convergence improves with increasing N^-, suggesting that the $-$ states are responsible for the slow convergence.

In fact, lowering the m^- mass improves the convergence. In Fig. 11, the black dots correspond to the extremal choice $m^-=m^+$ which, as we anticipated in Sec. I, is our final choice, and has been used in all calculations presented in this paper. With respect to the previous case, the convergence is much faster: the well-converged values at $N^++N^-=150$ (i.e., $N^+=N^-=75$) are obtained with $E^+_{\rm cut}=E^-_{\rm cut}=92.2$ meV; indeed, we find that the convergence nearly saturates when $E^+_{\rm cut}=E^-_{\rm cut}\gtrsim 85$ meV, i.e., just above the valence-band offset for this QWR. Note that, in addition to the improved convergence, the choice $m^-=m^+$ implies that only one of the two Eqs. (11a)–(11b) need to be solved.

As a final remark, we note that the convergence is slower for the eigenvalues at $k_z=0.02$ Å^{-1} than at $k_z=0$, due to the strong HH-LH mixing for large wave vectors. An accurate convergence at these wave vectors, as it can be achieved by our method, is, e.g., necessary to calculate in-wire effective mass at the Fermi wave vector. The slow convergence of the in-plane effective mass at the Fermi edge is a well-known problem in QW's.[32]

APPENDIX B: MATRIX ELEMENTS OF $\hat{\mathbf{H}}_L$

Once we have calculated the functions $\phi^+_\nu(x,y)$, $\phi^-_\mu(x,y)$, we compute the following integrals:

$$s(\nu,\mu)=\int_\Omega [\phi^+_\nu(x,y)]^*\phi^-_\mu(x,y)dx\ dy, \tag{B1a}$$

$$w_\beta(\nu,\mu)=\int_\Omega [\phi^+_\nu(x,y)]^*\hat{k}_\beta\phi^-_\mu(x,y)dx\ dy, \tag{B1b}$$

$$w_{\beta\beta'}(\nu,\mu)=\int_\Omega [\phi^+_\nu(x,y)]^*\hat{k}_\beta\hat{k}_{\beta'}\phi^-_\mu(x,y)dx\ dy, \tag{B1c}$$

$$v^+_\beta(\nu,\nu')=\int_\Omega [\phi^+_\nu(x,y)]^*\hat{k}^2_\beta\phi^+_{\nu'}(x,y)dx\ dy, \tag{B1d}$$

$$v^-_\beta(\mu,\mu')=\int_\Omega [\phi^-_\mu(x,y)]^*\hat{k}^2_\beta\phi^-_{\mu'}(x,y)dx\ dy, \tag{B1e}$$

where $\beta,\beta'\in\{x,y\}$. In our implementation, the functions ϕ^+_ν, ϕ^-_μ are expanded in plane waves. Although this is not necessary, it makes it very easy to compute the above integrals, where the operators $\hat{k}_\beta$ are just substituted by scalar numbers k_β.

With the above definitions, and using the short notations $s=s(\nu,\mu)$, $v^+_\beta=v^+_\beta(\nu,\nu')$, $v^-_\beta=v^-_\beta(\mu,\mu')$, $w_\beta=w_\beta(\nu,\mu)$, and $w_{\beta\beta'}=w_{\beta\beta'}(\nu,\mu)$, the only nonzero matrix elements of $\hat{\mathbf{H}}_L$ in the basis set (14a) and (14b) are

$$\langle +,\nu,\uparrow|\mathbf{H}_L|+,\nu',\uparrow\rangle=\left[\epsilon^+_\nu+\left(\gamma_1-\frac{\gamma_2-3\gamma_3}{2}\right)k_z^2\right]\delta_{\nu\nu'}+p_x^+v_x^++p_y^+v_y^+, \tag{B2a}$$

$$\langle +,\nu,\downarrow|\mathbf{H}_L|+,\nu',\downarrow\rangle=\langle +,\nu,\uparrow|\mathbf{H}_L|+,\nu',\uparrow\rangle, \tag{B2b}$$

$$\langle -,\mu,\uparrow|\mathbf{H}_L|-,\mu',\uparrow\rangle=\left[\epsilon^-_\mu+\left(\gamma_1+\frac{\gamma_2-3\gamma_3}{2}\right)k_z^2\right]\delta_{\mu\mu'}+p_x^-v_x^-+p_y^-v_y^-, \tag{B2c}$$

$$\langle -,\mu,\downarrow|\mathbf{H}_L|-,\mu',\downarrow\rangle=\langle -,\mu,\uparrow|\mathbf{H}_L|-,\mu',\uparrow\rangle, \tag{B2d}$$

$$\langle +,\nu,\uparrow|\mathbf{H}_L|-,\mu,\uparrow\rangle=-\frac{\sqrt{3}}{2}[2(\gamma_2w_{yy}-2i\gamma_3k_zw_y)-(\gamma_2+\gamma_3)k_z^2s-(\gamma_2-\gamma_3)w_{xx}], \tag{B2e}$$

$$\langle +,\nu,\downarrow|\mathbf{H}_L|-,\mu,\downarrow\rangle=-\frac{\sqrt{3}}{2}[2(\gamma_2w_{yy}+2i\gamma_3k_zw_y)-(\gamma_2+\gamma_3)k_z^2s-(\gamma_2-\gamma_3)w_{xx}], \tag{B2f}$$

$$\langle +,\nu,\downarrow|\mathbf{H}_L|-,\mu,\uparrow\rangle=2\sqrt{3}(\gamma_3w_{xy}+i\gamma_2k_zw_x), \tag{B2g}$$

$$\langle +,\nu,\uparrow|\mathbf{H}_L|-,\mu,\downarrow\rangle=-2\sqrt{3}(\gamma_3w_{xy}-i\gamma_2k_zw_x). \tag{B2h}$$

APPENDIX C: OPTICAL TRANSITION MATRIX ELEMENTS

We define the electron-hole overlap integrals

$$t^+(n,\nu)=\int_\Omega [\psi^e_n(x,y)]^*\phi^+_\nu(x,y)dx\ dy, \tag{C1}$$

$$t^-(n,\mu)=\int_\Omega [\psi_n^e(x,y)]^* \phi_\mu^-(x,y)dx\ dy. \tag{C2}$$

Then, the matrix elements for valence-to-conduction-band absorption, with light linearly polarized along the [110], [001], and $[\bar{1}10]$ directions, are the following.

Direction [110],

$$M_{\alpha\to n,\uparrow}=\sum_{J_m}\langle s,\uparrow|p_x|3/2,J_m\rangle\int [\psi_n^e(x,y)]^*\psi_{J_m}^h(x,y)dx\ dy$$
$$=-\frac{P}{\sqrt{2}}\left[\frac{2}{\sqrt{3}}\sum_\mu C_\alpha^-(\mu,\downarrow)t^-(n,\mu)\right], \tag{C3}$$

$$M_{\alpha\to n,\downarrow}=\sum_{J_m}\langle s,\downarrow|p_x|3/2,J_m\rangle\int [\psi_n^e(x,y)]^*\psi_{J_m}^h(x,y)dx\ dy$$
$$=-\frac{P}{\sqrt{2}}\left[\frac{2}{\sqrt{3}}\sum_\mu C_\alpha^-(\mu,\uparrow)t^-(n,\mu)\right]. \tag{C4}$$

Direction [001],

$$M_{\alpha\to n,\uparrow}=\sum_{J_m}\langle s,\uparrow|p_y|3/2,J_m\rangle\int [\psi_n^e(x,y)]^*\psi_{J_m}^h(x,y)dx\ dy$$
$$=\frac{P}{\sqrt{2}}\left[\sum_\nu C_\alpha^+(\nu,\uparrow)t^+(n,\nu)-\frac{1}{\sqrt{3}}\sum_\mu C_\alpha^-(\mu,\uparrow)t^-(n,\mu)\right], \tag{C5}$$

$$M_{\alpha\to n,\downarrow}=\sum_{J_m}\langle s,\downarrow|p_y|3/2,J_m\rangle\int [\psi_n^e(x,y)]^*\psi_{J_m}^h(x,y)dx\ dy$$
$$=\frac{P}{\sqrt{2}}\left[-\sum_\nu C_\alpha^+(\nu,\downarrow)t^+(n,\nu)+\frac{1}{\sqrt{3}}\sum_\mu C_\alpha^-(\mu,\downarrow)t^-(n,\mu)\right]. \tag{C6}$$

Direction $[\bar{1}10]$,

$$M_{\alpha\to n,\uparrow}=\sum_{J_m}\langle s,\uparrow|p_z|3/2,J_m\rangle\int [\psi_n^e(x,y)]^*\psi_{J_m}^h(x,y)dx\ dy$$
$$=\frac{iP}{\sqrt{2}}\left[\sum_\nu C_\alpha^+(\nu,\uparrow)t^+(n,\nu)+\frac{1}{\sqrt{3}}\sum_\mu C_\alpha^-(\mu,\uparrow)t^-(n,\mu)\right], \tag{C7}$$

$$M_{\alpha\to n,\downarrow}=\sum_{J_m}\langle s,\downarrow|p_z|3/2,J_m\rangle\int [\psi_n^e(x,y)]^*\psi_{J_m}^h(x,y)dx\ dy$$
$$=\frac{iP}{\sqrt{2}}\left[\sum_\nu C_\alpha^+(\nu,\downarrow)t^+(n,\nu)+\frac{1}{\sqrt{3}}\sum_\mu C_\alpha^-(\mu,\downarrow)t^-(n,\mu)\right]. \tag{C8}$$

[1] For a review, see, R. Cingolani and R. Rinaldi, Riv. Nuovo Cimento **16**, 1 (1993).

[2] E. Kapon, D.M. Hwang, and R. Bhat, Phys. Rev. Lett. **63**, 430 (1989).

[3] M. Gailhanou *et al.*, Appl. Phys. Lett. **62**, 1623 (1993).

[4] S. Tiwari *et al.*, Appl. Phys. Lett. **64**, 3536 (1994).

[5] R. Rinaldi *et al.*, Phys. Rev. B **50**, 11 795 (1994).

[6] M. Grundmann *et al.*, J. Nonlin. Opt. Phys. Mater. **4**, 99 (1995).

[7] L.N. Pfeiffer *et al.*, Appl. Phys. Lett. **56**, 1697 (1990).

[8] D. Gershoni *et al.*, Phys. Rev. Lett. **65**, 1631 (1990).

[9] H.L. Störmer *et al.*, Appl. Phys. Lett. **58**, 726 (1991).

[10] A.R. Goñi *et al.*, Appl. Phys. Lett. **61**, 1956 (1992).

[11] W. Wegscheider *et al.*, J. Cryst. Growth **150**, 285 (1995).

[12] H. Akiyama, T. Someya, and H. Sakaki, Phys. Rev. B **53**, R4229 (1996).

[13] H. Akiyama, T. Someya, and H. Sakaki, Phys. Rev. B **53**, R10 520 (1996); T. Someya, H. Akiyama, and H. Sakaki, Phys. Rev. Lett. **76**, 2965 (1996).

[14] W. Langbein, H. Gislason, and J. M. Hvam, Phys. Rev. B **54**, 14 595 (1996); H. Gislason, W. Langbein, and J. M. Hvam, Appl. Phys. Lett. **69**, 3248 (1996).

[15] P.C. Sercel and K.J. Vahala, Appl. Phys. Lett. **57**, 545 (1990).

[16] D.S. Citrin and Y.-C. Chang, Phys. Rev. B **40**, 5507 (1989).

[17] U. Bockelmann and G. Bastard, Europhys. Lett. **15**, 215 (1991); Phys. Rev. B **45**, 1688 (1992).

[18] D.S. Citrin and Y.-C. Chang, Phys. Rev. B **43**, 11 703 (1992).

[19] H. Ando, S. Nojima, and H. Kanbe, J. Appl. Phys. **74**, 6383 (1993).

[20] G. Goldoni and A. Fasolino, Phys. Rev. B **52**, 14 118 (1995); Physica B **211**, 444 (1995).

[21] A.A. Yamaguchi and A. Usui, J. Appl. Phys. **78**, 1361 (1995).

[22] F. Rossi and E. Molinari, Phys. Rev. Lett. **76**, 3642 (1996); Phys. Rev. B **53**, 16 462 (1996); in *The Physics of Semiconductors*, edited by M. Scheffler and R. Zimmermann (World Scientific, Singapore, 1996), p. 1161.

[23] G. Goldoni *et al.*, Appl. Phys. Lett. **69**, 2965 (1996).

[24] Note that the electron subband index n does not include spin, and two spin orientations correspond to each n, while for holes the index m includes the spin character.

[25] J.M. Luttinger, Phys. Rev. **102**, 1030 (1956).

[26] J.-B. Xia, Phys. Rev. B **43**, 9856 (1991).

[27] R. Rinaldi *et al.*, Phys. Rev. Lett. **73**, 2899 (1994).

[28] For holes, the word ''spin'' is used in a generalized way, and does not correspond to a well-defined spin orientation. See D.A. Broido and L.J. Sham, Phys. Rev. B **31**, 888 (1985); L.C. Andreani, A. Pasquarello, and F. Bassani, *ibid.* **36**, 5887 (1987); G. Goldoni and A. Fasolino, Phys. Rev. Lett. **69**, 2567 (1992); **69**, 2567 (1992).

[29] The QW subbands are calculated by a finite element solution of the Luttinger Hamiltonian in the relevant crystallographic direc-

tions. See J. Los, A. Fasolino, and A. Catellani, Phys. Rev. B **53**, 4630 (1996). Note that the QWR ground state is actually slightly above the QW2 continuum, contrary to the expectation for a localized level. Actually, this is a fictitious result due to the different accuracy between the plane-wave expansion of QWR states and the real-space representation used to calculate the QW states. In reality, the QWR ground state, being localized, lies slightly below the QW continuum. However, for this structure the binding energy is very small.

[30] G. Bastard, *Wave Mechanics Applied to Semiconductor Heterostructures* (Les Éditions des Physique, Les Ulis, Paris, France, 1988).

[31] U. Bockelmann and G. Bastard, Phys. Rev. B **45**, 1700 (1992).

[32] T. Ando, J. Phys. Soc. Jpn. **54**, 1528 (1985).